

Classification: Physical Sciences: Earth, Atmospheric and Planetary Sciences.

Title: Precursory moment release scales with earthquake magnitude.

Authors: M. Acosta^{1*}, F.X. Passelègue¹, A. Schubnel², R.Madariaga², M. Violay¹

Affiliations:

¹EPFL, LEMR, Lausanne, Switzerland,

²Laboratoire de Géologie, CNRS, UMR, ENS, Paris, FR.

*Correspondence to: mateo.acosta@epfl.ch. ORCID#0000-0002-0098-7912.

Abstract:

Today, observations of earthquake precursors remain widely debated. While precursory slow slip is an important feature of earthquake nucleation, foreshock sequences are not always observed and their temporal evolution remains unconstrained. Here, we report on stick-slip experiments (laboratory earthquakes) conducted under seismogenic stresses in dry and fluid pressure conditions. We show that the precursory moment release scales with mainshock magnitude irrespective of the slip behavior (seismic or aseismic), the presence of fluid and the fault's slip history. Importantly, this observation is supported by earthquake nucleation theory and holds for natural earthquakes in a magnitude range from $M_w6.0$ to $M_w9.0$. Even though a large gap remains between laboratory and natural observations, moderate to large earthquakes may be foresighted through integrated seismological and geodetic measurements of both seismic and aseismic slip during earthquake nucleation.

Keywords : Earthquake Nucleation; Laboratory Earthquakes; Fault Coupling; Precursory Moment release.

Significance Statement:

Understanding the slow nucleation phase preceding dynamic earthquake ruptures is crucial to assess seismic hazard. Here, we show that the temporal evolution of laboratory earthquake precursors (precursory slow slip, fault coupling and precursory seismicity) are of little use to assess seismic hazard. Nevertheless, irrespective of fault slip behavior (seismic or aseismic) and environmental conditions (stress state; fluid pressure and slip history), the amount of moment released during the precursory phase scales with earthquake magnitude. This property is demonstrated by laboratory observations, earthquake nucleation theory and, by natural

observations of earthquakes ranging from M_w 6.0 to M_w 9.0. Larger earthquakes must therefore exhibit a larger nucleation phase and consequently are more likely to be detectable.

Main Text:

Understanding earthquake initiation is crucial to assessing seismic hazard. Theoretical and numerical models using either slip-weakening laws (1-3) or rate and state friction laws (4-7) predict that earthquake rupture is preceded by a nucleation phase (NP). The rupture accelerates over a growing fault patch until it reaches a characteristic length L_c , at which dynamic rupture propagation initiates. While the NP has been studied in the laboratory (2, 8-13), natural observations of such NP are scarce and remain debated (14-17). The study of recent well-instrumented moderate and large magnitude earthquakes has highlighted that several ruptures were preceded by precursory slip, linked or not with foreshock sequences (16-21). However, other observations indicate that, rather than precursory slip, foreshocks trigger one another in a cascade-like manner up to the main rupture (15). This debate remains unresolved mainly because the temporal evolution of both slip and seismicity and their intensity compared to the mainshock remain poorly constrained. The answers to the above questions might be found at the laboratory scale, where rupture propagation and fault conditions are well-controlled.

Here, we carefully analyzed the NP of 150+ laboratory stick-slip events (proxies for earthquakes) conducted under stress conditions representative of the upper seismogenic crust, under both dry and pressurized fluid conditions. We conducted experiments at confining pressures (σ_3) ranging between 50 to 95 MPa and pore fluid pressures (p_f) from 0 to 60 MPa. In each case, the displacement-stress curve (Fig.1a,c., *Methods*) revealed an initial elastic loading phase until a stress state τ_s . Then, the fault started to slip in a stable manner (2, 10, 11). When precursory slip (u_{prec}) finished, the fault's maximum shear strength (σ_0) was reached and the

instability propagated with fast co-seismic slip (u_{cos}) and a sudden stress drop ($\Delta\sigma_{\text{cos}}$) down to a final stress value (σ_f). When co-seismic slip arrested, as constant loading continued, a new elastic loading phase ensued, repeating the stick-slip cycle (Fig.1).

Under dry conditions (Fig.1a,b), the NP is characterized by an exponential slip acceleration following $u_{\text{prec}}(t)=u_0*\exp((t_0-t)/t_c)$ where t_0 is the time of the mainshock, t_c the characteristic nucleation time (9), and u_0 is fault slip at the beginning of the acceleration phase. Note that both temporal constants can be estimated only after the mainshock occurrence. Analysis of acoustic emissions activity (AEs) in our experiments (*Methods*) highlights that, under dry conditions, AEs also followed an exponential increase until (t_0) (Fig.1b insert), consistent with the exponential acceleration of u_{prec} (13). Subsequent stick-slip events led to an increase of the total AEs (from 31 in cycle #1 to 79 in cycle #10). With pressurized fluids (Fig.1c, d), the NP is characterized by two clearly distinguishable slip acceleration stages. The first one is described by an exponential acceleration as observed in dry conditions. However, a transition from an exponential growth to a power law is observed close to dynamic rupture propagation. This change in acceleration of u_{prec} is comparable to the nucleation process observed through high-speed photo-elasticity in transparent polymers (9). There, the length of the ruptured area within the nucleation zone patch grew first exponentially with time, and, once the size of the rupture patch became comparable to that of the characteristic nucleation length, the growth followed as an inverse power law of time. This second slip acceleration stage can be very short during dry experiments; potentially the reason why it was not observed. Surprisingly, with pressurized fluids, u_{prec} was not associated with any AEs. It is unlikely that the absence of foreshocks in all fluid-pressurized conditions resulted solely from increased attenuation of seismic waves since the sensors were located <1 mm away from the fault. Previous experiments

have indeed shown that AEs are systematically observed prior to the failure of intact or thermally cracked, dry or water saturated granite specimens (22).

To further investigate the NP of laboratory earthquakes (Fig.2), we computed the temporal evolution of the fault's mechanical coupling (FC , *Methods*, Ref.24) as a function of time to mainshock during earthquake sequences recorded both in dry and water-pressurized conditions. As expected, the fault remained strong ($FC \sim 1$) during elastic loading. At the onset of the mainshock, $FC(t_0)$ decreased to ~ 0.85 - 0.7 due to initiation of the nucleation process in dry conditions. With subsequent events, $FC(t_0)$ decreased due to fault surface evolution (Fig2. darkest traces; Ref.10). With pressurized fluids, when nucleation initiated, FC consistently decreased to ~ 0.5 at t_0 . No influence of the sliding history and fault surface evolution was noted. The reduced fault coupling and lack of foreshocks (or their size reduction) under fluid pressure conditions could be due to a local increase of the nucleation length at the scale of fault's asperities. The presence of local fluid overpressures influences the dynamics of fault's asperities by changing the distribution of frictional heterogeneities which in turn control both fault coupling and foreshock dynamics (6,7).

We now estimate the moment release of both the precursory and co-seismic stages (Fig.3a, *Methods*). While the temporal evolution of slip and seismicity during nucleation depends on the fault's state of stress (13), fluid pressure level and cumulative fault slip, we observe that in our experiments M_p systematically scales with M_0 (i.e. the magnitude of the instability) (Fig.3a). The scaling can be shown combining earthquake nucleation theory with the scaling between earthquakes' fracture energy and co-seismic slip. In fact, experimental (2,24-25), seismological (26) and theoretical studies (27) have demonstrated that the fracture energy of earthquakes increases as a power law of their co-seismic slip following: $G = a u_{cos}^\alpha$, where a is a scaling

pre-factor, and α a given power (in our experiments $\alpha \sim 1.22e10$ and $\alpha \sim 1.783$ (Fig.S4, *Methods*)).

G can then be used in a small-scale-yielding description to estimate an upper-end value of the nucleation length (1-3) following: $L_c = \frac{2\mu G}{\Delta\sigma_d^2}$, with $\Delta\sigma_d$ the earthquake's dynamic stress drop.

Then, using usual seismological relations (*Methods*), we get the following scaling relation between precursory and co-seismic moments:

$$M_p = \frac{(2a \cdot \mu^{1-\alpha})^3}{C^{2\alpha}} \cdot \frac{\Delta\sigma_s^{2\alpha}}{\Delta\sigma_d^5} \cdot M_0^\alpha \quad (Eq1)$$

This relationship shows that the larger the released precursory moment, the larger the co-seismic moment of the earthquake. Taking common stress drop values in our experiments ($\Delta\sigma_s = 2$ to 40 MPa and $\Delta\sigma_d = 5$ to 90 MPa, Table.S1) we observe that this relation quantitatively predicts the precursory moment release observed in our experiments. Note that such $\Delta\sigma_s$ and $\Delta\sigma_d$ values are higher than usual earthquake stress drops, due to our finite experimental fault and fixed rupture area. In laboratory earthquakes, most of the elastic energy is accumulated in the apparatus column, i.e. within a volume considerably larger than the sample. The larger the normal stress (σ_{N0}) acting on the fault, the larger the elastic energy stored within the sample/apparatus medium and consequently, the larger the coseismic slip and fracture energy if compared to an infinite fault. Therefore, increasing σ_{N0} in our experiments does not necessarily imply a reduction of L_c (2,4,6,9,13) because of the larger $\Delta\sigma_s$ and $\Delta\sigma_d$. In our experiments, the scaling arises from the relation between u_{prec} and u_{cos} (Fig.S4) and it is noteworthy that u_{prec} , u_{cos} , $\Delta\sigma_s$, and $\Delta\sigma_d$ evolved spontaneously when faults reached the conditions for instability. Therefore, the scaling between M_p and M_0 resulted from the final value of these four quantities, resulting in values for α slightly larger than those of natural observations (25-26). The scaling is also confirmed on mechanical

data obtained by previous studies of laboratory earthquakes (Fig.3a, empty symbols, Methods), highlighting the independence from the experimental set-up.

While the precursory moment release remains undetermined in most natural and anthropogenic seismicity (28), several examples of well-instrumented earthquakes where the NP is properly characterized follow the same scaling relation as our laboratory earthquakes. This is especially valid when geodetic and/or repeater inferred measurements of precursory moment release are taken into account (Fig3.b, black squares; *Methods*, Refs:17, 19-21, *Supplementary References*). In addition, considering M_p only from the release of seismic moment during foreshock sequences (i.e. only from seismic slip) results in large undershoot with respect to the proposed scaling (Fig3.b red star (18)). If the proposed scaling property is correct, this undershoot could occur because part of the precursory deformation is accommodated by aseismic slip transients (17, 19-22) or by seismic events of magnitude smaller than the magnitude of completeness of the catalogs. While this feature is clearly observed in laboratory experiments (Fig.1-3, Refs: 2, 8-13), natural observations of aseismic slip are still rare and debated (14-17). In the light of our results and because current geodesy generally lacks the resolution to observe aseismic slip (14, 17), some earthquake sequences may nevertheless present a cascade-like initiation (i.e. small events trigger one another until the main rupture (15)). Yet, where transients of aseismic slip can be resolved, earthquakes seem to nucleate through a slow slip trigger (16-17, 19-21). When considering precursory aseismic slip, experimental and seismological observations suggest that M_p , i.e. the energy released during NP, increases with the seismic moment of the mainshock. In fact, applying $Eq1$ with the scaling proposed by Abercrombie and Rice (Ref:26; ($\alpha \sim 1.28$ and $a = 5.25e6$)) and usual (29) earthquake stress drops ($\Delta\sigma_s \sim 0.1-1$ MPa and $\Delta\sigma_d = 1-10$ MPa) our scaling provides conservative estimates for natural earthquakes (Fig.3b, dotted lines).

Our study has strong implications for earthquake nucleation. First, because the precursory moment release systematically follows an exponential growth during the first acceleration phase, continuously monitoring the time evolution of fault coupling could provide first order information about the fault's stability, and the eventual rupture initiation. Second the occurrence of a large earthquake (M_w7 or higher) does not necessarily imply that a larger earthquake will not occur in the days following it. If the released seismic moment contributes to the precursory moment for a bigger asperity, a larger earthquake can occur in a close timescale, as was the case for the 2011 $M_w9.0$ Tohoku-Oki (20), the 2014 $M_w8.1$ Iquique (21) and the 1960 $M_w9.4-9.6$ Valdivia (30) earthquakes, all of which were preceded by large M_w foreshocks. Third, and foremost, independent of initial conditions (fluid pressure, stress and slip history), the larger M_p , the larger M_0 (Fig. 3) whether it is released seismically, aseismically or by a combination of both. This confirms that both the number of foreshocks and their characteristic acceleration can differ for a given earthquake magnitude (19). Moreover, fluid pressures are likely to reduce fault coupling (17,31), compared to dry conditions, and, in light of our experiments, regulate foreshock sequences. Significantly, M_p increases with mainshock magnitude. Therefore, the larger the fault patch which will rupture, the larger L_c and the higher the possibility of detecting and following precursory activity of moderate to large earthquakes by combined geodetic and seismological methods.

Materials and Methods

Starting samples

Experimental samples consisted of Westerly Granite (WG) cylinders of 40 mm diameter and 88 mm length. WG is a material representative of the upper continental crust and suitable for laboratory work due to its low alteration, low anisotropy, homogeneity, fine grain size and

simple mineralogy. The cylinders were initially heat-treated at 450°C in order to increase their permeability by one order of magnitude ($\sim 10^{-19} \text{ m}^2$) and consequently, to allow reasonable fluid diffusion and saturation times. Cylinders were then saw-cut at an angle (θ) of 30° to the sample's long axis to create an artificial elliptical fault ($\sim 80 \text{ mm}$ length and $\sim 40 \text{ mm}$ width). The fault's surfaces were grinded to ensure perfect contact and roughened with #240 grit paper in order to ensure a minimum cohesion along the fault's interface and impose a constant fault roughness in all the specimens.

Triaxial apparatus and pore fluid system

Experiments were performed on the oil-medium, tri-axial apparatus of ENS Paris. The apparatus is able to support 100 MPa in confining pressure and 680 MPa in axial stress for samples of 40 mm diameter. Both axial and confining stresses were servo-controlled independently and recorded with 1 kPa resolution. Fluid pressures were servo-regulated through a *Quizix 20k* double syringe pump of 120 MPa maximum capacity (1 microliter and 1 kPa volume and pressure accuracy). Axial displacements (u_{ax}) were recorded through three gap sensors located outside the cell with a resolution of 0.1 μm at 100 samples per second.

Acoustic emission monitoring

During experiments, acoustic activity was monitored through 15 piezo-ceramic sensors which consist of a PZT crystal (PI ceramic PI255, 0.5 mm thick and of diameter 5 mm) contained in a brass casing. The sensors were glued directly on the samples with cyanoacrylate adhesive following the sensor map in Fig.S1. Acoustic waveforms were recorded with two different techniques (13). First, each unamplified signal was relayed to a digital oscilloscope allowing for the recording of macroscopic stick-slip events within a time window of 6.5 ms at 10 MHz (13). Second, to record low amplitude acoustic emissions activity, signals were amplified at

45 dB through pre-amplifiers. Amplified signals were then relayed to a trigger logic box. Using this second system, AE's were recorded if at least 4 sensors recorded an amplitude larger than a given threshold, that is set at 0.001 Volts. The complete waveform catalogue was then manually analyzed to remove possible triggers from background noise.

High frequency stress and strain monitoring

Four strain gauges shown in Fig.S1. were glued ~1 mm away from the fault and allowed a local recording of the axial (ϵ_1) and radial (ϵ_3) strains at 10 MHz sampling frequency. The gauges were wired in a full (Wheatstone) bridge configuration, allowing the direct measurement of ϵ_1 - ϵ_3 through the $4 \times 350 \Omega$ resistors. To calibrate the gauges, we assumed a constant Young's modulus of the rock during the elastic loading phase of each event such that we had direct conversion from the strain recorded at the gauge to the corresponding far field differential stress ($\Delta\sigma$). This near-fault sensor allowed recording the dynamic character of each stick-slip event (32) and therefore to estimate the fracture energy of the event (24).

Loading procedure

For each test, axial and radial pressures (respectively (σ_1) and (σ_3)) were increased up to 10 MPa. Then, in the case of pore fluid experiments, air was cautiously flushed from the sample by increasing fluid pressure (p_f) at the lower end of the sample. Once fluid percolated through the entire sample, fluid pressure was increased up to 5 MPa at the upper and lower ends until pressure and volume equilibrium were reached at both ends. Experiments were then conducted at different effective pressure conditions, where $\sigma' = \sigma - p_f$ accounts for effective stress. Finally, axial stress was increased imposing a constant volume rate in the axial piston which resulted in initial strain rates- ranging from $\sim 1.10^{-5} \text{ s}^{-1}$ to $\sim 3.10^{-5} \text{ s}^{-1}$ while (σ_3) and (p_f) were held constant. Under

our experimental configuration, the fault's shear stress (τ) and effective normal stress (σ_n') were computed following:

$$\tau = \frac{\sigma_1' - \sigma_3'}{2} * \sin(2\theta) \quad (Eq2)$$

and

$$\sigma_n = \frac{\sigma_1' - \sigma_3'}{2} * (1 - \cos 2\theta) + \sigma_3' \quad (Eq3)$$

Due to our experimental configuration, shear and normal stresses increased simultaneously as σ_1' increased.

Fault displacement (u_f) was computed from the gap sensors located outside the pressure vessel by correcting the direct measurement of axial displacement (u_{ax}) from the stiffness of the experimental apparatus ($E_{y_{col}} \sim 38$ GPa) and by projecting the displacement on the fault plane following:

$$u_f = \frac{u_{ax} - E_{y_{col}} * L * \Delta\sigma}{\cos\theta} \quad (Eq4)$$

where L is the sample's length; and $\Delta\sigma$ is the deviatoric stress.

A summary of the 150+ recorded stick-slip events is presented in Supplementary Table 1. In these experiments, radial stresses ranged from 50 to 95 MPa and pore fluid pressures from 0 to 60 MPa.

Mechanical coupling of experimental faults

To evaluate the degree of mechanical coupling of the experimental fault during stick-slip cycles (FC), we first computed the fault slip rate (\dot{u}_f) recorded using the external gap sensors with 1 s centered time windows such that:

$$\dot{u}_f(t) = \frac{u(t + 0.5 \text{ s}) - u(t - 0.5 \text{ s})}{((t + 0.5 \text{ s}) - (t - 0.5 \text{ s}))} \quad (Eq5)$$

Due to the fast strain rates imposed in our experiments compared to tectonic loading rates, we assumed that all deviations in strain rate from a fully coupled fault resulted from slip along the fault (IO). Then, we defined the mechanical coupling of the fault as the ratio between the estimated fault slip rate to the imposed displacement rate when the fault is fully coupled (\dot{u}_0) such that: $FC = \left(\frac{\dot{u}_f}{\dot{u}_0}\right)$. This estimation of the fault coupling is comparable with the one derived from geodetic measurements along natural faults (23, 33).

Corrections for elastic displacement and calculation of precursory and co-seismic moment in laboratory earthquakes.

In all our experiments (Table.S1), the corrections for elastic displacement of the sample and apparatus deformation were performed replacing E_{ycol} in (Eq4). by a new constant $E_{y\text{system}}$ which was computed individually for each event. In that sense, the change in elasticity was corrected after each dynamic slip event. For the external points (Refs. 34-36 the data was manually

recovered. Then, the data were corrected for elasticity and the shear stress –slip curves were plotted (examples are shown in Fig.S2.). Values of maximum shear stress at the onset of instability (τ_0), shear stress drop ($\Delta\sigma$), precursory slip (u_{prec}) and co-seismic slip (u_{cos}) were recovered from those curves (Fig. S2.) and reported in Table.S2. From that table, the precursory and co-seismic moments were computed as $M_p = \mu.A.u_{\text{prec}}$ and $M_0 = \mu.A.u_{\text{cos}}$ respectively taking an average rock shear modulus of $\mu=30$ GPa (Fig. S3.)

Precursory and co-seismic moment release: Theory.

From a theoretical viewpoint, assuming that NP ends with a linear slip weakening law similar to dynamic rupture, the precursory moment can be written as $M_p = \mu.D_c.L_c^2$, where D_c is the characteristic slip weakening distance. The earthquake's fracture energy is $G = \frac{\Delta\sigma_d D_c}{2}$ with $\Delta\sigma_d$ the earthquake's dynamic stress drop. G can then be used in a small-scale-yielding description to estimate an upper end value of the nucleation length ($l,3$) following: $L_c = \frac{\mu D_c}{\Delta\sigma_d}$. From these relationships we get a scaling between the precursory moment M_p , the stress drop, and the fracture energy G:

$$M_p = \frac{(2\mu G)^3}{\Delta\sigma_d^5} \quad (\text{Eq6})$$

The seismic moment is $M_0 = \mu.u_{\text{cos}}.L^2$ and the co-seismic static stress drop is $\Delta\sigma_s = C.\mu.\frac{u_{\text{cos}}}{L}$, where C is a geometric factor equal to 7/16 for a circular crack and μ the rock's shear modulus (37). From these two relationships, we get:

$$u_{cos} = \frac{\Delta\sigma_s^{\frac{2}{3}} M_0^{\frac{1}{3}}}{\mu C^{\frac{2}{3}}} \quad (Eq7)$$

Experimental (2,24,25), seismological (26) and theoretical studies (27) demonstrated that the fracture energy of earthquakes increases as a power law of their co-seismic slip, which is a proxy for the rupture length and can be written as:

$$G = a u_{cos}^\alpha \quad (Eq8)$$

Where a is a scaling pre-factor, and α a given power. In our experiments, we find $a \sim 1.22e10$ and $\alpha \sim 1.783$ (Fig.S4.).

Combining equations (Eq6)-(Eq8), we get the following scaling relation between precursory and co-seismic moments:

$$M_p = \frac{(2a \cdot \mu^{1-\alpha})^3}{C^{2\alpha}} \cdot \frac{\Delta\sigma_s^{2\alpha}}{\Delta\sigma_d^5} \cdot M_0^\alpha \quad (Eq1)$$

References and Notes:

1. Ida, Y. Cohesive force across the tip of a longitudinal-shear crack and Griffith's specific surface energy. *J. Geophys. Res.*, **77(20)**, 3796–3805. (1972)
2. Ohnaka, M. *The physics of rock failure and earthquakes*. Cambridge University Press. (2010).
3. Campillo, M., Ionescu, I. R. Initiation of antiplane shear instability under slip dependent friction. *J. Geophys. Res.*, 102(B9), 20363-20371 (1997)
4. Rubin, A.M., Ampuero, J.P., Earthquake nucleation on (aging) rate and state faults. *J. Geophys. Res.*, 110(B11). (2005).
5. Lapusta, N., Rice, J.R., Nucleation and early seismic propagation of small and large events in a crustal earthquake model. *J. Geophys. Res.*, 108(B4). (2003).
6. Dublanchet, P. The dynamics of earthquake precursors controlled by effective friction. *Geophys. J. Int.*, **212(2)**, 853–871. (2018)
7. Yabe, S. and Ide, S., Variations in precursory slip behavior resulting from frictional heterogeneity. *Prog. Earth. Plan. Sci.*, 5(1), p.43. (2018)
8. Dieterich, J.H., Preseismic fault slip and earthquake prediction. *J. Geophys. Res.*, 83(B8), pp.3940-3948. (1978)
9. Latour, S., et al., Characterization of nucleation during laboratory earthquakes. *Geophys. Res. Lett.*, **40(19)**, 5064–5069. (2013). <https://doi.org/10.1002/grl.50974>
10. Scholz, C., et al., Detailed studies of frictional sliding of granite and implications for the earthquake mechanism. *J. Geophys. Res.*, **77(32)**, 6392–6406. (1972)

11. Byerlee, J.D., Summers, R. Stable sliding preceding stick-slip on fault surfaces in granite at high pressure. *Pageoph.*, **113**. (1975)
12. McLaskey, G., C., Lockner, D. A. Preslip and cascade processes initiating laboratory stick slip. *J. Geophys. Res.*, **119(8)**, 6323–6336. (2014).
13. Passelègue, F. X., et al., Influence of Fault Strength on Precursory Processes During Laboratory Earthquakes. *Geophys. Mon.* **227**, 229–242. (2017)
14. Gomberg, J., Unsettled Earthquake Nucleation. *Nat. Geosc.*, **11**, 463–464 (2018)
15. Ellsworth, W.L., Bulut, F., 2018. Nucleation of the 1999 Izmit earthquake by a triggered cascade of foreshocks. *Nat. Geosc.*, **11**, 531–535 (2018)
16. Tape, C., et al., Earthquake nucleation and fault slip complexity in the lower crust of central Alaska. *Nat. Geosc.*, **11**, 536–541 (2018)
17. Voss, N., et al., Do slow slip events trigger large and great megathrust earthquakes?. *Sci. adv.*, **4(10)**. (2018)
18. Bouchon, M., et al., Extended nucleation of the 1999 Mw 7.6 Izmit earthquake. *Science*, **331(6019)**, 877–880. (2011)
19. Bouchon, M., et al., The long precursory phase of most large interplate earthquakes. *Nat. Geosci.*, **6(4)**, 299–302. (2013)
20. Kato, A., et al., Propagation of Slow Slip Leading Up to the 2011 Mw 9.0 Tohoku-Oki Earthquake. *Science*, **335(6069)**, 705–708. (2012)
21. Socquet, A., et al., An 8-month slow slip event triggers progressive nucleation of the 2014 Chile megathrust. *Geophys. Res. Lett.*, **44(9)**, 4046–4053. (2017)

22. Wang, X.Q., et al., Physical properties and brittle strength of thermally cracked granite under confinement. *J. Geophys. Res.*, 118(12), pp.6099-6112. (2013)
23. Métois, M., et al. Interseismic coupling, segmentation and mechanical behavior of the central Chile subduction zone. *J. Geophys. Res.*, **117**(3). (2012).
24. Passelègue, F., et al., Dynamic rupture processes inferred from laboratory microearthquakes. *J. Geophys. Res.*, 121(6), pp.4343-4365. (2016).
25. Nielsen, S., et al., G: Fracture energy, friction and dissipation in earthquakes. *J. seism.*, 20(4), pp.1187-1205. (2016)
26. Abercrombie, R.E., Rice, J.R., Can observations of earthquake scaling constrain slip weakening?. *Geophys. J. Int.*, 162(2), 406-424. (2005)
27. Viesca, R.C., Garagash, D.I., Ubiquitous weakening of faults due to thermal pressurization. *Nat. Geosci.*, 8(11), p.875. (2015)
28. Guglielmi, Y., et al., Seismicity triggered by fluid injection–induced aseismic slip. *Science*, 348(6240), pp.1224-1226. (2015)
29. Twardzik, C., Das, S., Madariaga, R., Inversion for the physical parameters that control the source dynamics of the 2004 Parkfield earthquake. *J. Geophys. Res.*, 119(9), pp.7010-7027. (2014).
30. Barrientos S.E.; Ward S.N. The 1960 Chile earthquake: inversion for slip distribution from surface deformation. *Geophys. J. Int.* 103 (3): 589–598. (1990).
31. Moreno, M., et al. Locking of the Chile subduction zone controlled by fluid pressure before the 2010 earthquake. *Nat. Geosci.*, **7**(4), 292–296. (2014)

32. Acosta, M., Passelègue, F.X., Schubnel, A. and Violay, M., Dynamic weakening during earthquakes controlled by fluid thermodynamics. *Nat. Comms.*, 9(1), p.3074. (2018)
33. Savage, J. C., A dislocation model of strain accumulation and release at a subduction zone, *J. Geophys. Res.*, 88 (B6), 4984-4996 (1983).
34. Summers, R., Byerlee, J.D., Summary of results of frictional sliding studies at confining pressures up to 6.98 kb. in selected rock materials., *U.S. Geol. Surv. Open File Rep.*, **129**, 77-142. (1977). <https://doi.org/10.3133/ofr77142>
35. McLaskey, G. C., Lockner, D. A., Shear failure of a granite pin traversing a sawcut fault. *Int. J. Rock Mech. Min. Sci.*, **110**, 97-110. (2018).
<https://doi.org/10.1016/j.ijrmms.2018.07.001>
36. Lockner, D.A., et al. The transition from frictional sliding to shear melting in laboratory stick-slip experiments., *Geophys. Mon.*, **227**, (2017).
37. Kanamori, H., Brodsky, E.E., The physics of earthquakes. *Rep. Prog. Phys.*, 67(8), 1429. (2004).
38. Borghi, A., et al., Precursory slow-slip loaded the 2009 L'Aquila earthquake sequence. *Geophys. J. Int.*, 205(2), 776-784. (2016).
39. Shelly, D.R., Possible deep fault slip preceding the 2004 Parkfield earthquake, inferred from detailed observations of tectonic tremor. *Geophys. Res. Lett.* (2009) 36(17).
40. Radiguet, M., et al., Triggering of the 2014 M w 7.3 Papanoa earthquake by a slow slip event in Guerrero, Mexico. *Nat. Geosc.*, 9(11), 829. (2016)
41. Huang, H. and Meng, L., Slow Unlocking Processes Preceding the 2015 Mw 8.4 Illapel, Chile, Earthquake. *Geophys. Res. Lett.*, 45(9), 3914-3922. (2018)

42. Ruiz, S., et al., Intense foreshocks and a slow slip event preceded the 2014 Iquique Mw8.1 earthquake. *Science*, (6201), 1165–1169. (2014)
43. Graham, S.E., et al., GPS constraints on the 2011–2012 Oaxaca slow slip event that preceded the 2012 March 20 Ometepepec earthquake, southern Mexico. *Geophys. J. Int.*, 197(3), pp.1593-1607. (2014)
44. Ruegg, J.C., Olcay, M., Lazo, D., Co-, post-and pre (?) seismic displacements associated with the Mw 8.4 Southern Peru earthquake of 23 June 2001 from continuous GPS measurements. *Seis. Res. Lett.*, 72(6), pp.673-678. (2001).
45. Ruiz, S., et al., Nucleation phase and dynamic inversion of the Mw 6.9 Valparaíso 2017 earthquake in Central Chile. *Geophys. Res. Lett.*, (2017) 44(20).
46. <http://www.seismo.ethz.ch/en/earthquakes/monitoring/geothermal-energy-basel/List-of-Earthquakes>.

Acknowledgments: M.A. and M.V. acknowledge the funding support from the Swiss National Science Foundation (SNF), project no. PYAPP2160588, and the technical staff at LEMR for help with sample preparation and Barnaby Fryer for proofreading the manuscript. M.V. acknowledges the European Research Council Starting Grant project 757290-BEFINE. A.S acknowledges the European Research Council, grant no. 681346-REALISM. F.X.P. acknowledges funding from the SNF, project no. PZENP2173613. M.A., M.V. and A.S. also acknowledge the Germaine de Staël French-Swiss exchange program.

Author Contributions:

Supplementary Information:

Supplementary Methods

Fig S1 – S5

Table S1 – S3

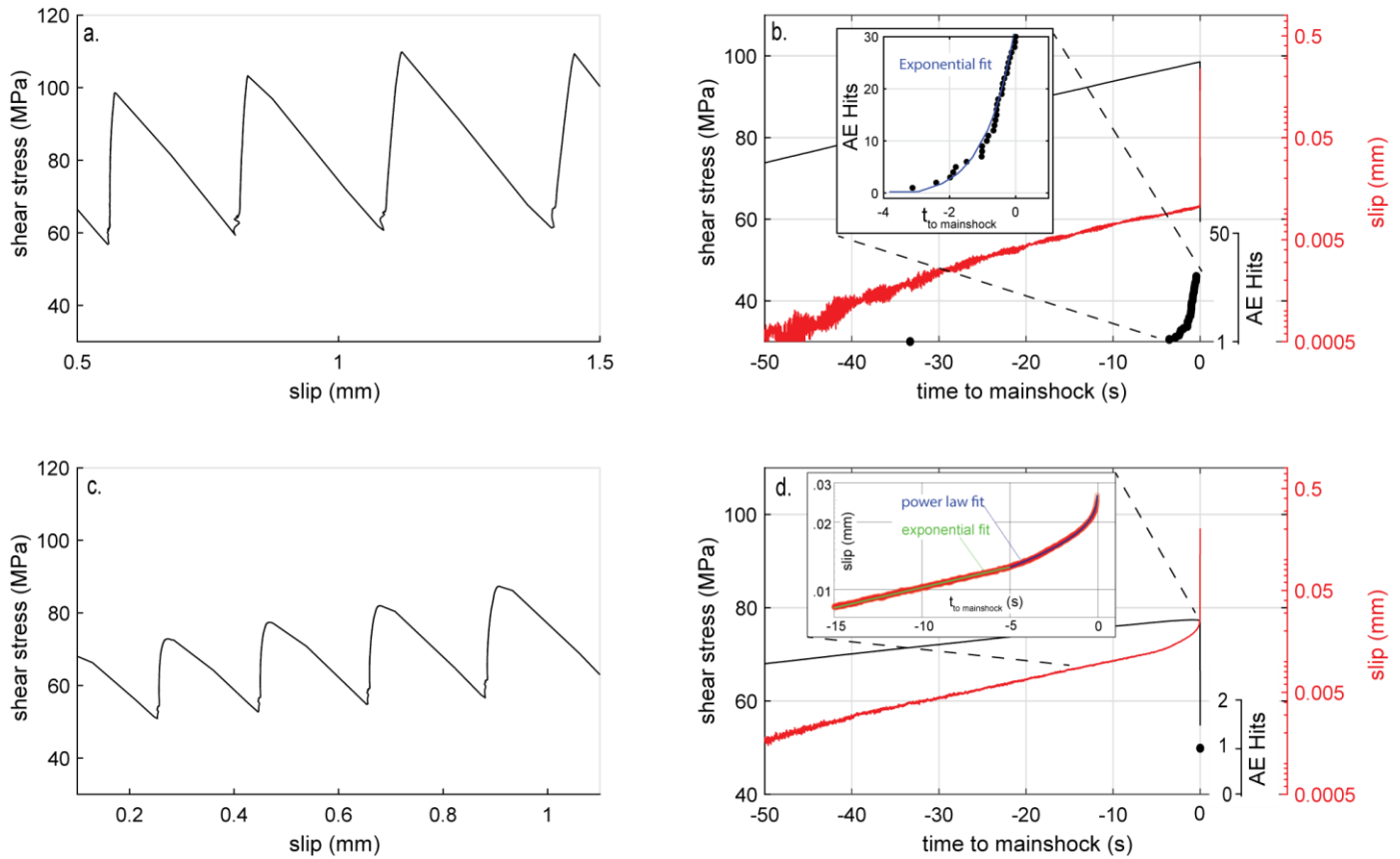


Figure.1. Stick-slip experiments.

a,c. Shear stress vs. on-fault slip for experiments run at confining pressure $\sigma_3' = 70$ MPa. **a.** Dry experiment, **c.** Experiment at fluid pressure $p_f = 1$ MPa. **b,d.** Shear stress (black line), fault slip (red line in log scale) and AE's (black dots) for one stick slip cycle vs. time to mainshock (t_0). **b.** Dry experiment. Inset shows a close-up of AE's from t_0-4 s with exponential fit. **d.** Experiment at $p_f = 1$ MPa. Only acoustic emission arrival was the mainshock. Inset shows exponential fit for the first nucleation stage from t_0-15 s to t_0-5 s as: $u(t) = 0.015 \cdot \exp(t_0 - t) / 23.8$ in green. In addition, in blue, a power law fit from t_0-5 s to t_0 as: $u(t) = u(t_0-5s) - 0.0116 \cdot t^{0.254}$.

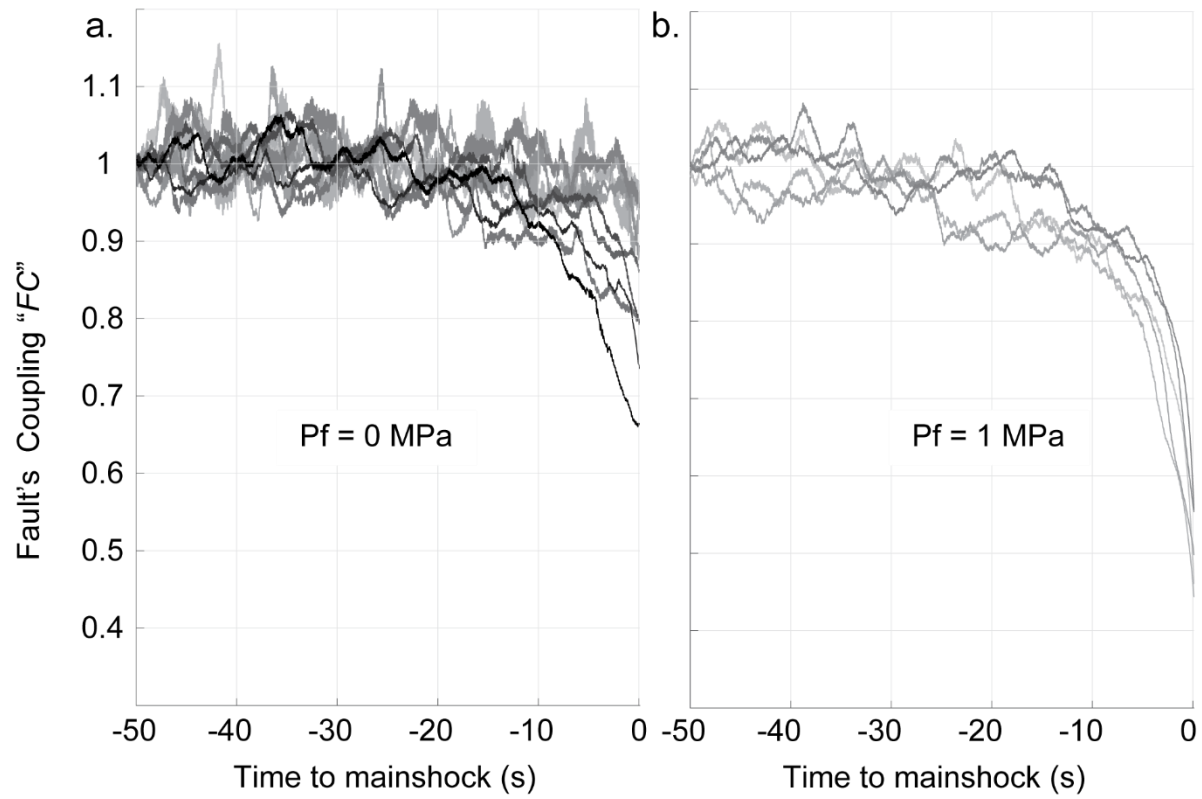


Figure. 2. Fault coupling prior to mainshock for single stick-slip cycles.

Fault coupling (*Methods*) vs. time to mainshock for experiments at $\sigma_3' = 70$ MPa. **a.** Dry experiments **b.** With pressurized fluid ($p_f = 1$ MPa). Darkest traces correspond to later events.

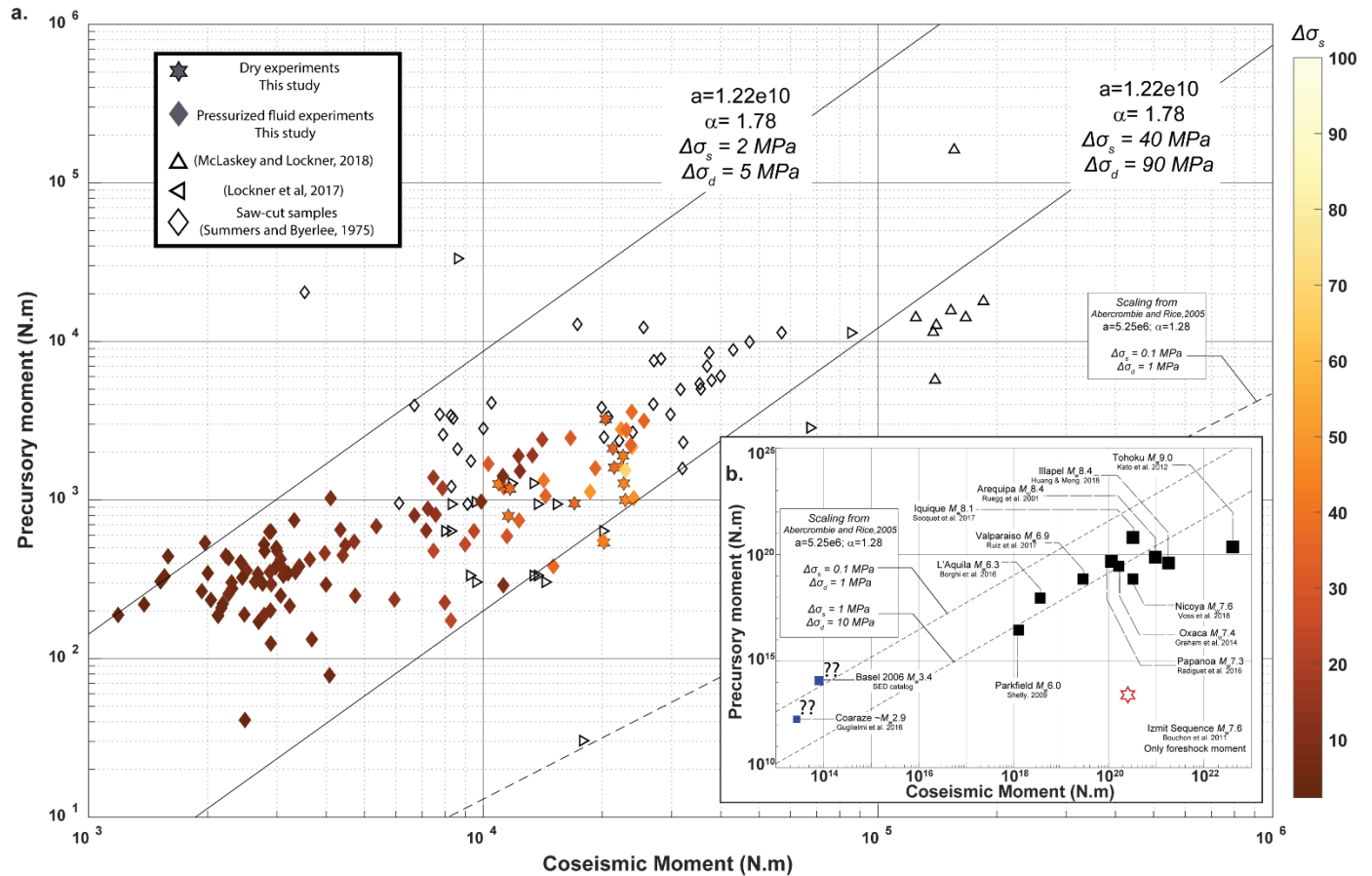


Figure 3. Earthquake moment release in natural and laboratory earthquakes.

a. Precursory vs Co-seismic moment release for all stick-slip cycles analyzed from the laboratory. Color bar represents static shear stress drop. Empty symbols account for external points. Black lines account for the scaling using (Eq1) with $\alpha=1.783$ and $a=1.22e10 \text{ J.m}^{2+\alpha}$. b. Data for natural earthquakes. Full squares account for M_p inferred from integrated analysis of a combination of geodetic, and/or seismic precursory moment release. Blue squares represent induced events (Methods). Red star corresponds to the Izmit sequence (18) and accounts for all 18 foreshock moment release. Black dashed lines correspond to M_0 vs. M_p from Eq1 using the scaling from Ref:26 with $\alpha=1.28$ and $a=5.25e6$.

Supplementary Information for

Precursory moment release scales with earthquake magnitude.

M. Acosta, F.X. Passelègue, A. Schubnel, R. Madariaga, M. Violay

Correspondence to: mateo.acosta@epfl.ch

This PDF file includes:

Supplementary Methods

Figs. S1 to S5

Tables S1 to S3

Supplementary Methods

Precursory and co-seismic moment release in natural Earthquakes.

To compute the precursory and co-seismic moment release for natural earthquakes different methods were used in the literature and are detailed below for each point of Figure.3b. The values for M_p and M_0 are given in Table.S3. Note that in this analysis, we assume that all the recorded precursory slow slip contributes to the nucleation of the mainshock, therefore, the spatiotemporal frame taken for nucleation is the largest possible in all cases.

- 2009 M_w 6.3 L'Aquila Earthquake from *Borghiet al. (2016)*, Ref.38.

Borghiet al. analyzed continuous GPS stations and detected an SSE (Slow Slip Event) that started on the 12 February and lasted for almost two weeks prior to the 2009 M_w 6.3 L'Aquila Earthquake. From their analysis, the authors estimated a total precursory magnitude for the SSE of M_w 5.9 which resulted in a precursory moment release, $M_p \sim 10^{(3/2(5.9+6.07))} = 9.02e17$ N.m. For this earthquake we have $M_0 \sim 10^{(3/2(6.3+6.07))} = 3.59e18$ N.m.

- 2011 M_w 9.0 Tohoku-Oki Earthquake from *Kato et al. (2012)* Ref.20.

In their work, Kato et al. (2012) used a waveform correlation technique on the earthquake catalog preceding the 2011 M_w 9.0 Tohoku-Oki Earthquake in order to identify migrating foreshocks towards the epicenter of the mainshock. They inferred the temporal evolution of quasi static slip of the plate interface based on small repeating earthquakes. From this analysis, the authors estimate a total aseismic moment release by slow slip transients of M_w 7.1 over the area hosting foreshock distributions. This results in $M_p \sim 10^{(3/2(7.1+6.07))} = 4.47e19$ N.m and $M_0 \sim 10^{(3/2(9.0+6.07))} = 3.16e22$ N.m.

- 2014 M_w 8.1 Iquique Earthquake from *Socquet et al. (2017)* Ref:21.

Socquet et al. (2017) analyzed the acceleration recorded at a group of GPS stations located in Coastal Northern Chile. This acceleration started 8 months prior to the 2014 M_w 8.1 Iquique Earthquake. They showed that this acceleration corresponded to a first M_w 6.5 slow slip event on the Chilean subduction interface, which was followed by a large M_w 6.7 foreshock. That foreshock further generated a M_w 7.0 afterslip event which finally ruptured the area of the M_w 8.1 mainshock. From their analysis, we estimate the total precursory moment release as the sum of these events, resulting in $M_p \sim 10^{(3/2(6.5+6.07))} + 10^{(3/2(6.7+6.07))} + 10^{(3/2(7.0+6.07))} = 7.16e18 + 1.43e19 + 4.03e19 = 6.17e19$ N.m. and we have $M_0 \sim 10^{(3/2(8.1+6.07))} = 1.80e21$ N.m.

- 2004 M_w 6.0 Parkfield Earthquake *Shelly (2009)*, Ref:39

In his work, Shelly (2009) used observations of deep tremors in order to infer slow slip preceding the 2004 M_w 6.0 Parkfield Earthquake. The author observed elevated tremor rates in the 3 months preceding the mainshock \sim 16km beneath the hypocenter and concluded that the deep slip interacted with the mainshock area for that earthquake. From the tremor rate analysis, the author proposes (under several assumptions) that the slow slip event prior to the mainshock had a M_w 4.9. This results in $M_p \sim 10^{(3/2(4.9+6.07))} = 2.85e16$ N.m and $M_0 \sim 10^{(3/2(6.0+6.07))} = 1.27e18$ N.m.

- 2014 M_w 7.3 Papanoa Earthquake from *Radiguet et al. (2016)*, Ref :40.

In the work of Radiguet et al. (2016), the authors reconstructed the aseismic slip evolution on the subduction interface of the Guerrero segment through inversion of GPS position time series. The authors found a slow slip of total moment magnitude M_w 7.6 that began two months prior to the 2014 M_w 7.3 Papanoa earthquake. This slow slip event persisted for \sim 9 months after the Papanoa

earthquake. The authors studied the temporal evolution of moment release during the slow slip event and found that, prior to the Papanoa earthquake, around 15% of the moment release corresponding to the $M_w7.6$ slow slip event had been released at the time of the earthquake.

Using the moment magnitude scale, this results on an estimation for

$M_p \sim 0.15 \cdot 10^{(3/2(7.6+6.07))} = 7.77 \cdot 10^{19}$ N.m and $M_0 \sim 10^{(3/2(7.3+6.07))} = 8.91 \cdot 10^{19}$ N.m.

- 2015 $M_w8.4$ Illapel Earthquake from *Huang and Meng. (2018)*, Ref:41

Huang and Meng (2018), Propose that the 2014 Illapel earthquake was preceded by a progressively accelerating aseismic slip phase. Such analysis is done through a matched-filter technique which allowed for the identification of repeating earthquakes. Then, from repeating earthquake analysis, the authors propose that an area of 50.50 km² presented an average slip of ~30 cm in a time period of several months prior to the mainshock. Such an observation, assuming a rock's shear modulus of 30 GPa, results in an estimated $M_p \sim 30 \cdot 10^9 \cdot (50 \cdot 10^3)^2 \cdot 0.3 = 2.25 \cdot 10^{19}$ N.m and $M_0 \sim 10^{(3/2(8.4+6.07))} = 5.07 \cdot 10^{21}$ N.m.

-2012 Nicoya $M_w7.6$ earthquake from *Voss et al. (2018)*, Ref:17

Analyzing the slip and seismicity that preceded the 2012 Nicoya $M_w7.6$ Earthquake, Voss et al. were able to study data from 20+ GPS stations which were located in a peninsular area and therefore close to the mainshock's epicenter. From their analysis, the authors propose that a Slow Slip Event started 6 months prior to the mainshock. They conclude that the coulomb frictional stress change prior to the mainshock was low and therefore they discard a cascade-like nucleation process. The authors estimate the precursory moment release to an equivalent $M_w6.5$ event which results in an estimated $M_p \sim 7.16 \cdot 10^{18}$ N.m and $M_0 \sim 3.20 \cdot 10^{19}$ N.m.

In addition, the authors compile a number of earthquakes where precursory aseismic slip was observed (their supplementary Table S1) from which we have plotted the additional points in figure 3 from Refs: 21,42-44.

-2017 $M_w6.9$ Valparaiso Earthquake from *Ruiz et al. (2018)* Ref: 45.

In their work, Ruiz et al. studied the nucleation phase through GPS and repeater type seismicity of the 2017 $M_w6.9$ Valparaiso earthquake. They conclude that most of the precursory deformation phase was aseismic (80% of the precursory seismic moment) and they estimate the precursory moment release to an equivalent $M_w6.55$ event which results in an estimated $M_p \sim 8.51 \cdot 10^{18}$ N.m and $M_0 \sim 2.85 \cdot 10^{19}$ N.m.

-2006 Basel $M_w3.2$ Earthquake from SED catalog Ref:46

Through the precise catalog of the Swiss seismological service (SED) with a magnitude of completion $M_w1.4$, we identify all seismic events that occurred prior to the December 8th 2006 $M_w3.2$ induced earthquakes that occurred in Basel. Because of the low magnitude of completion and the small spatial distribution of seismic events (Haring et al., 2008), it is reasonable to assume that all the recorded events can contribute to the nucleation of the largest event. We therefore sum up the magnitudes of all recorded events prior to the mainshock and estimate $M_p = 1.22 \cdot 10^{14}$ N.m and $M_0 = 8.04 \cdot 10^{13}$. (SED website reference).

-Coaraze induced earthquakes from *Guglielmi et al. (2015)*, Ref:28

In the study by *Guglielmi et al., (2015)*, the authors performed semi-controlled hydraulic injections into a natural fault and recorded the fault's response in terms of slip and seismicity. From their Figure 1, a precursory aseismic slip event precedes the occurrence of micro seismicity and a slip acceleration phase. While in this study a mainshock cannot be clearly defined, we assume that the whole slip event without any seismicity contributes to precursory moment release and the second – seismic-- slip phase contributes to co-seismic moment release. From their mechanical data and modelling, the authors estimate a 15 m radius for the precursory

slipping zone and a total precursory slip of 35 cm. For the 'co-seismic slip phase', the authors estimate a 35 m radius for the second slipping zone and a total slip of 95 cm. From this, considering the shear modulus of the rock to be 30 GPa, we estimate $M_p = 1.86 \times 10^{12}$ N.m and $M_p = 2.74 \times 10^{13}$ N.m.

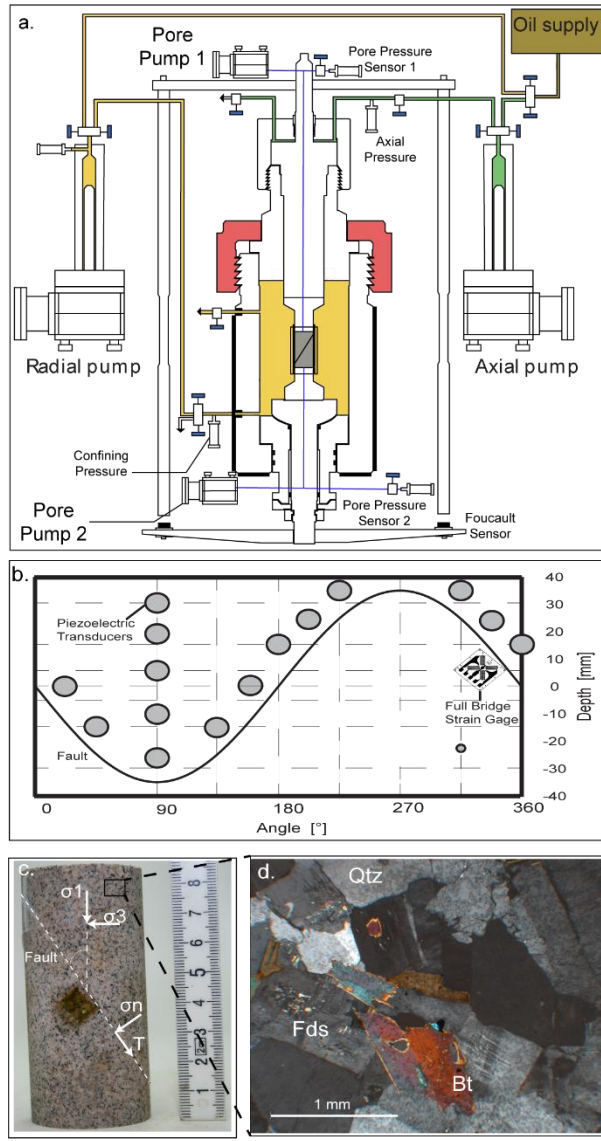


Fig. S1. Experimental set-up.

a. Triaxial apparatus. **b.** Acoustic emission sensor and strain gage map. **c.** Westerly Granite saw-cut cylinder and stress distribution. **d.** Westerly Granite microstructure under cross-polarized optical microscopy.

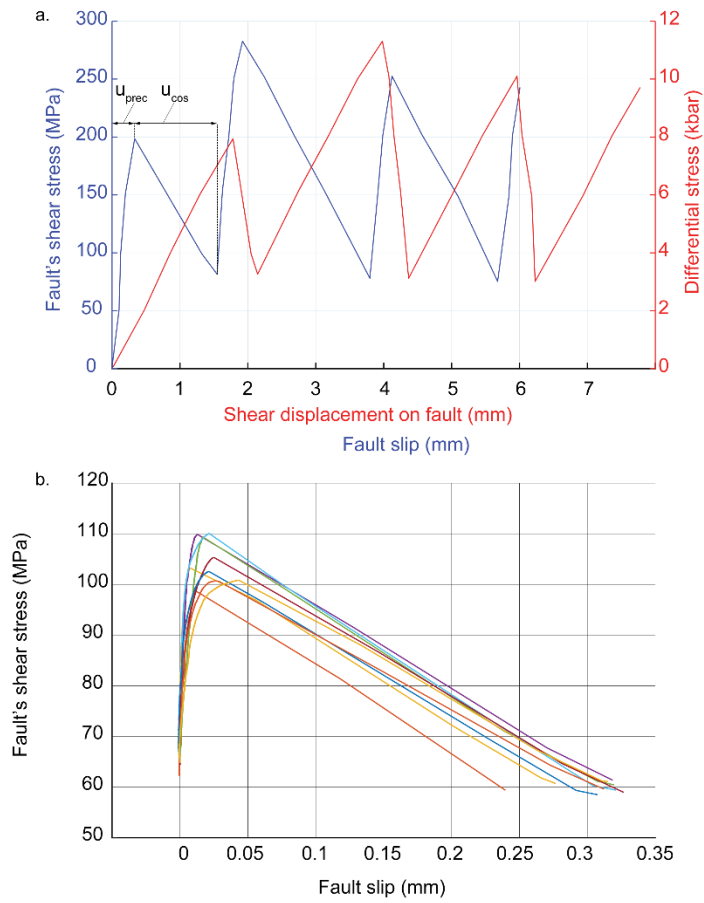


Fig. S2. Corrections for elasticity.

a. Red curve, extracted raw data for intact rock from ref (*Summers and Byerlee, 1975*). Blue curve: same dataset corrected from elastic deformation to get only fault slip and on-fault shear stress (Methods). Examples are shown of u_{prec} and u_{cos} values in the first event. **b.** Example of dataset from our experiments. Corrections for elasticity account for the change in shear stiffness for every event.

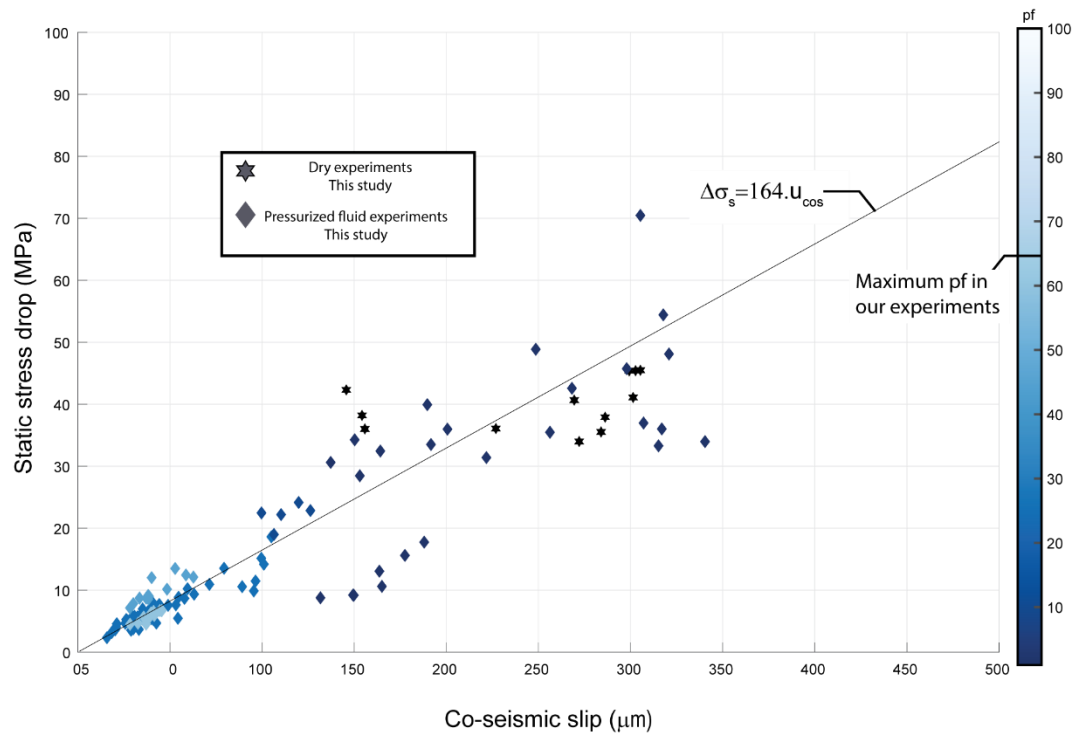


Fig. S3. Static Stress drop versus co-seismic slip.

Black stars represent dry experiments. Diamonds represent experiments with pressurized fluids. Pore fluid pressure in color bar. Black line represents $\Delta\sigma_s = 164 \cdot u_{cos}$ which gives a shear modulus of 30 GPa for the fault with the circular crack approximation.

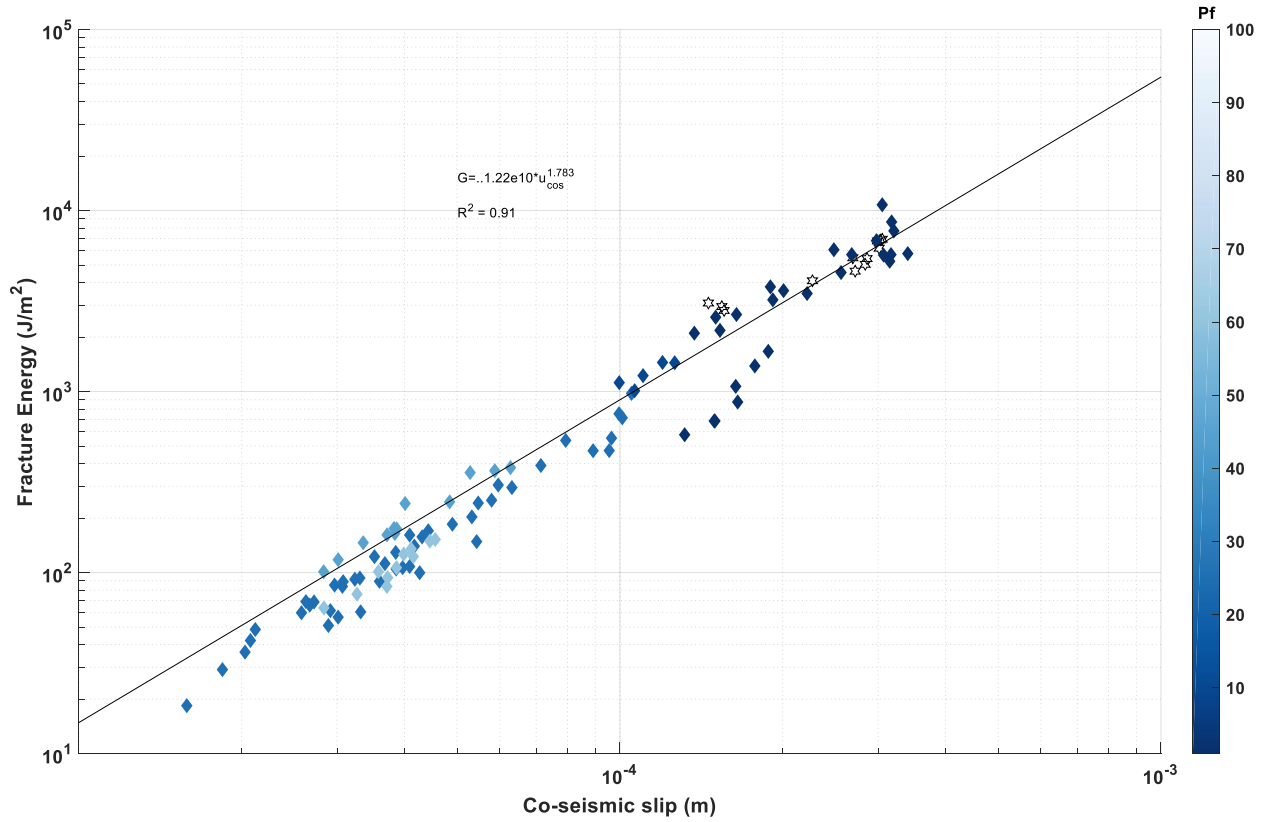


Fig. S4. Scaling between fracture energy and co-seismic slip.

Black stars represent dry experiments. Diamonds represent experiments with pressurized fluids. Pore fluid pressure in color bar. Black line represents $G = 1.22e10 \cdot u_{\text{cos}}^{1.783}$, which is the best fit to the data points.

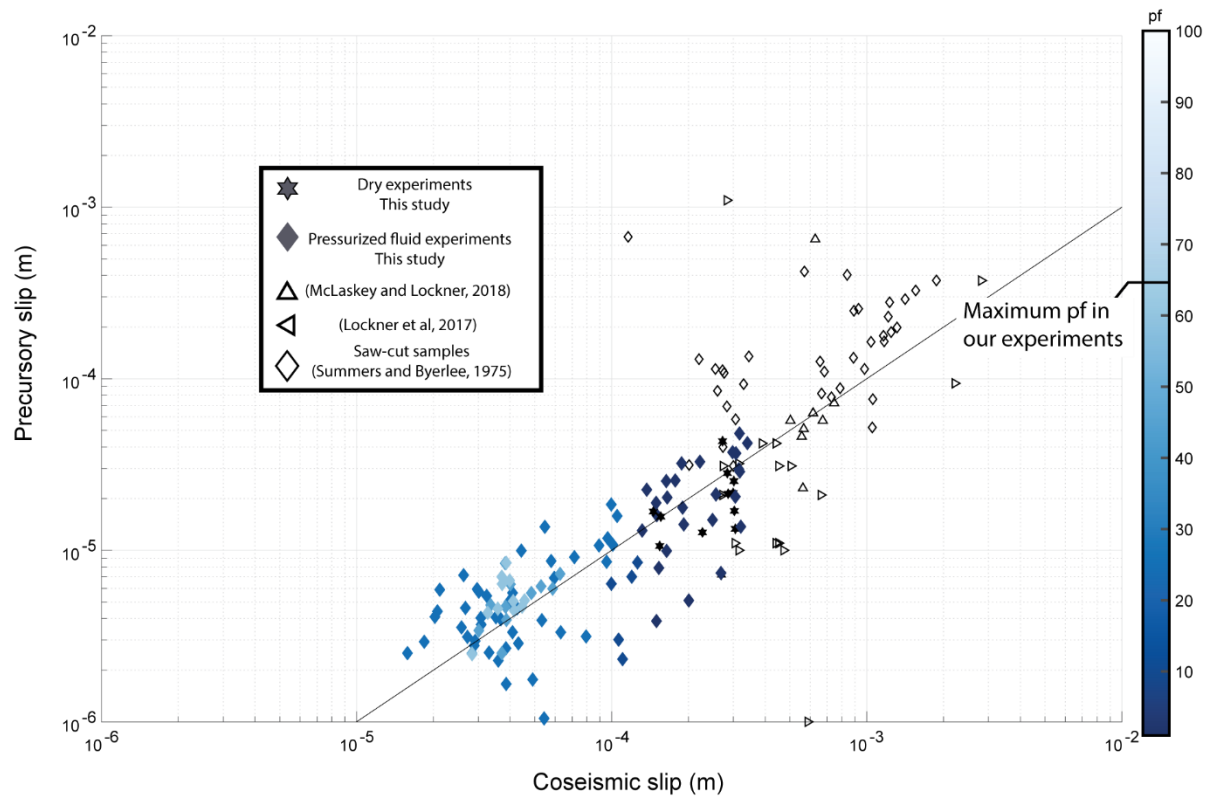


Fig. S5. Precursory and co-seismic slip relation.

Precursory fault slip as a function of co-seismic fault slip. Diamonds account for data from our experiments in presence of fluid pressures shown in the color bar. Black stars account for data from our dry experiments. All other symbols account for external data reported in Supplementary table 2. Black line accounts for $u_{\text{prec}}=0.1 u_{\text{cos}}$.

Table S1. Experimental data from this study.

Experiment	σ_3	Pf	σ_3'	$E_{ySystem}$	u_{prec}	u_{cos}	$\Delta\sigma_s$	$\Delta\sigma_a$	G'
Name	MPa	MPa	MPa	MPa	μm	μm	MPa	MPa	J.m ⁻²
WG702	70	0	70	47500	12.7	226.9	36.07	76.10	8633.86
WG703	70	0	70	45000	7.2	269.4	40.66	82.27	11083.38
WG704	70	0	70	43500	13.3	305.3	45.47	91.16	13916.84
WG705	70	0	70	43000	17.0	302.7	45.41	83.40	12623.10
WG706	70	0	70	40500	21.6	299.3	45.38	91.07	13626.96
WG707	70	0	70	40500	25.3	301.4	41.08	84.76	12772.22
WG708	70	0	70	38500	21.4	286.2	37.90	76.28	10916.02
WG709	70	0	70	38000	28.2	284.0	35.51	79.17	11242.28
WG710	70	0	70	38000	43.3	272.1	33.98	73.94	10059.81
WG5401	95	25	70	66500	2.8	28.9	3.53	14.38	207.99
WG5402	95	25	70	72500	3.0	29.2	4.23	16.79	244.80
WG5403	95	25	70	70500	5.7	30.1	3.76	14.71	221.65
WG5404	95	25	70	70500	1.7	38.6	5.42	17.04	328.72
WG5405	95	25	70	68500	2.7	38.5	6.71	18.51	356.43
WG5406	95	25	70	68500	4.6	42.6	4.68	19.59	417.63
WG5407	95	25	70	68500	4.6	41.7	6.71	20.52	427.69
WG5408	95	25	70	68000	3.7	30.8	5.78	18.01	277.27
WG5409	95	25	70	68000	0.5	33.2	3.66	20.63	342.12
WG5410	95	25	70	68000	1.8	49.0	7.55	24.68	604.84
WG5411	95	25	70	68000	8.7	57.9	8.67	22.92	663.78
WG5412	95	25	70	72500	1.0	54.4	5.45	27.40	744.77
WG5413	95	25	70	64500	3.1	79.4	13.53	34.04	1351.33
WG5414	95	25	70	64500	8.6	95.5	9.87	38.27	1828.25
WG5415	95	25	70	66500	18.5	99.6	15.13	41.50	2067.25
WG5416	95	25	70	66500	15.8	105.1	18.60	38.81	2038.57
WG5501	95	1	94	80000	22.5	137.3	30.60	73.52	5046.04
WG5502	95	1	94	77000	16.0	150.3	34.25	85.67	6437.83
WG5503	95	1	94	74000	17.7	189.7	39.92	87.68	8316.70
WG5504	95	1	94	66000	15.0	248.6	48.86	95.81	11907.25
WG5505	95	1	94	64000	20.5	305.4	70.45	103.48	15798.84
WG5506	95	1	94	60000	13.7	320.9	48.10	98.09	15736.73
WG5507	95	1	94	58000	7.4	268.2	42.56	94.62	12688.52
WG5508	95	1	94	56000	28.7	317.8	54.41	92.98	14772.78
WG5509	95	1	94	56000	37.3	297.9	45.73	83.84	12488.74
WG9401	70	0	70	57000	16.8	145.7	42.30	84.62	6165.93
WG9402	70	0	70	54500	10.6	154.3	38.19	84.91	6549.57

Experiment	σ_3	Pf	σ_3'	$E_{ySystem}$	u_{prec}	u_{cos}	$\Delta\sigma_s$	$\Delta\sigma_a$	G'
Name	MPa	MPa	MPa	MPa	μm	μm	MPa	MPa	J.m ⁻²
WG9403	70	0	70	57000	15.7	155.8	36.01	74.49	5802.90
WG10101	95	25	70	40000	2.5	15.8	2.32	14.34	113.55
WG10102	95	25	70	37000	2.9	18.4	3.16	16.51	152.04
WG10103	95	25	70	40000	4.1	20.3	3.58	17.95	182.00
WG10104	95	25	70	41000	4.4	20.8	4.06	18.73	194.40
WG10105	95	25	70	41000	5.9	21.2	4.58	19.09	202.27
WG10106	95	25	70	37000	3.6	25.8	4.65	17.06	220.01
WG10107	95	25	70	40000	4.6	26.7	4.95	16.90	225.73
WG10108	95	25	70	40000	3.1	27.2	5.06	19.36	263.28
WG10109	95	25	70	40000	7.2	26.3	5.26	19.19	252.19
WG10110	95	25	70	40000	4.0	30.7	5.46	23.22	356.41
WG10111	95	25	70	38000	2.5	33.1	5.64	19.13	316.20
WG10112	95	25	70	40000	5.9	29.7	5.74	22.96	340.80
WG10113	95	25	70	40000	5.4	32.4	5.67	24.24	392.22
WG10114	95	25	70	40000	2.3	35.9	4.98	20.21	363.16
WG10115	95	25	70	40000	4.1	35.2	6.96	20.37	358.39
WG10116	95	25	70	40000	4.0	36.8	6.09	21.68	398.71
WG10117	95	25	70	40000	3.3	40.9	5.29	27.22	556.10
WG10118	95	25	70	41000	2.9	43.1	7.30	22.43	483.34
WG10119	95	25	70	43000	5.6	40.9	7.89	22.53	460.42
WG10120	95	25	70	43000	5.0	39.7	5.37	22.21	440.43
WG10121	95	25	70	43000	3.3	63.1	9.34	29.18	921.37
WG10122	95	25	70	43000	3.9	53.3	7.62	27.41	729.87
WG10123	95	25	70	45000	10.0	44.2	7.69	27.41	606.35
WG10124	95	25	70	45000	6.9	59.6	10.22	23.22	691.69
WG10125	95	25	70	52000	13.7	54.7	8.85	28.59	782.21
WG10126	95	25	70	47000	9.1	71.4	10.93	35.47	1266.82
WG10127	95	25	70	47000	10.7	89.2	10.56	33.18	1480.05
WG10128	95	25	70	47000	11.8	96.5	11.46	31.51	1519.70
WG10129	95	25	70	47000	10.8	101.0	14.18	34.19	1726.81
WG10201	95	45	50	50000	3.4	30.1	7.81	23.56	355.18
WG10202	95	45	50	58000	2.5	28.3	7.13	21.44	303.93
WG10203	95	45	50	53000	4.8	33.5	8.71	22.97	385.21
WG10204	95	45	50	54000	2.5	37.1	8.70	27.07	502.30
WG10205	95	45	50	54000	3.9	38.7	9.01	25.92	501.22
WG10206	95	45	50	54000	6.3	40.1	12.01	26.75	536.22
WG10207	95	45	50	59000	4.7	38.4	8.57	33.21	637.13
WG10208	95	45	50	61000	8.4	38.2	9.15	26.37	504.27

Experiment	σ_3	Pf	σ_3'	$E_{ySystem}$	u_{prec}	u_{cos}	$\Delta\sigma_s$	$\Delta\sigma_a$	G'
Name	MPa	MPa	MPa	MPa	μm	μm	MPa	MPa	J.m ⁻²
WG10209	95	45	50	53000	5.6	48.4	10.14	31.61	765.73
WG10210	95	45	50	53000	6.2	52.9	13.49	28.52	753.84
WG10211	95	45	50	51000	6.0	58.7	12.44	29.88	877.07
WG10212	95	45	50	50000	7.3	62.8	12.10	36.16	1134.83
WG10501	95	60	35	37000	2.5	28.4	4.50	18.04	255.90
WG10502	95	60	35	42000	4.3	32.7	4.65	15.65	255.54
WG10503	95	60	35	39000	4.6	35.8	5.65	21.81	390.32
WG10504	95	60	35	41000	6.4	37.2	5.04	18.47	343.55
WG10505	95	60	35	40000	7.0	37.1	4.52	27.22	504.94
WG10506	95	60	35	41000	8.4	38.6	5.50	16.01	309.18
WG10507	95	60	35	39000	4.5	41.5	5.91	23.35	484.62
WG10508	95	60	35	43000	6.7	39.8	6.34	23.25	463.26
WG10509	95	60	35	40000	5.0	41.1	6.56	19.45	399.94
WG10510	95	60	35	37000	5.1	45.6	6.69	21.02	478.97
WG10511	95	60	35	40000	4.7	44.5	6.70	21.75	484.31
WG10601	95	10	85	56500	6.4	99.7	22.46	52.96	2640.43
WG10602	95	10	85	56500	3.0	106.5	18.98	60.75	3233.94
WG10603	95	10	85	55500	2.3	110.3	22.19	59.21	3267.07
WG10604	95	10	85	55500	7.0	119.9	24.14	56.96	3414.20
WG10605	95	10	85	55500	8.5	126.3	22.83	51.02	3220.82
WG10701	95	1	94	51500	7.9	153.1	28.45	113.58	8693.15
WG10702	95	1	94	50500	9.9	164.2	32.44	77.04	6325.86
WG10703	95	1	94	48500	14.1	191.7	33.50	114.68	10992.15
WG10704	95	1	94	46000	5.1	200.6	35.97	93.77	9406.92
WG17101	51	1	50	34500	3.9	149.8	9.17	96.79	7250.74
WG17102	51	1	50	36000	13.0	131.7	8.76	78.64	5178.75
WG17103	51	1	50	36000	18.9	149.4	9.20	89.73	6702.57
WG17201	71	1	70	34000	20.3	165.1	10.60	59.61	4920.05
WG17202	71	1	70	38500	25.3	163.7	13.05	104.30	8536.63
WG17203	71	1	70	38500	25.5	177.6	15.60	78.68	6985.21
WG17204	71	1	70	40000	32.1	188.0	17.74	93.73	8811.08
WG17205	71	1	70	39500	32.8	221.8	31.38	116.85	12956.90
WG17301	95	1	94	38500	21.2	256.3	35.47	90.86	11641.93
WG17302	95	1	94	41000	36.8	307.1	36.96	115.99	17809.10
WG17303	95	1	94	41000	29.7	315.2	33.28	164.32	25895.63
WG17304	95	1	94	42000	42.1	340.4	33.96	119.86	20401.38
WG17305	95	1	94	42500	48.0	317.0	36.01	119.86	18995.91

Table S2. External Data from Laboratory Earthquakes.

Study	Event	σ_3	Diameter	u_{prec}	u_{cos}	$\Delta\sigma_s$
Reference	Name	MPa	m	μm	μm	MPa
Lockner et al 2017	Event1	100	0.0254	1097	283	44.37
Lockner et al 2017	Event2	100	0.0254	42	388	53.62
Lockner et al 2017	Event3	100	0.0254	21	661	93.47
Lockner et al 2017	Event4	100	0.0254	1	587	80.79
Lockner et al 2017	Event5	100	0.0254	11	304	45.56
Lockner et al 2017	Event6	100	0.0254	10	472	73.79
Lockner et al 2017	Event7	100	0.0254	42	440	68.64
Lockner et al 2017	Event8	100	0.0254	11	451	71.54
Lockner et al 2017	Event9	100	0.0254	31	273	43.82
Lockner et al 2017	Event10	100	0.0254	11	440	71.56
Lockner et al 2017	Event11	100	0.0254	31	504	81.95
Lockner et al 2017	Event12	100	0.0254	10	315	53.61
Lockner et al 2017	Event13	100	0.0254	31	451	74.94
Lockner et al 2017	Event14	100	0.0254	32	314	50.8
Lockner et al 2017	Event15	100	0.0254	21	263	48.98
Lockner et al 2017	Event16	100	0.0254	21	272	47.85
Lockner et al 2017	Event1	100	0.0254	373.4	2810.6	343.248
Lockner et al 2017	Event2	100	0.0254	94	2213	286.648
McLaskey & Lockner 2018	DSC1	80	0.0726	650	628	30.94
McLaskey & Lockner 2018	DSC2	80	0.0726	46	556	31.91
McLaskey & Lockner 2018	DSC3	80	0.0726	72	745	43.74
McLaskey & Lockner 2018	DSC4	80	0.0726	57	502	28.23
McLaskey & Lockner 2018	DSC5	80	0.0726	63	616	36.93
McLaskey & Lockner 2018	DSC6	80	0.0726	51	566	33.98
McLaskey & Lockner 2018	DSC7	80	0.0726	57	672	40.34
McLaskey & Lockner 2018	DSC8	80	0.0726	23	562	33.24
Summers Byerlee 1977	Fig85-Evt1	398	0.0254	671.4	116	9.29
Summers Byerlee 1977	Fig85-Evt2	398	0.0254	31.4	201.2	14.28
Summers Byerlee 1977	Fig85-Evt3	398	0.0254	69	283	22.14
Summers Byerlee 1977	Fig85-Evt4	398	0.0254	31	300	27.85
Summers Byerlee 1977	Fig85-Evt5	398	0.0254	40	273	24.28
Summers Byerlee 1977	Fig85-Evt6	398	0.0254	108	276	27.84
Summers Byerlee 1977	Fig85-Evt7	398	0.0254	93	329	28.56
Summers Byerlee 1977	Fig85-Evt8	398	0.0254	112	272	30.71
Summers Byerlee 1977	Fig85-Evt9	398	0.0254	135	345	30.7
Summers Byerlee 1977	Fig85-Evt10	398	0.0254	85	260	25.71

Study	Event	σ_3	Diameter	u_{prec}	u_{cos}	$\Delta\sigma_s$
Reference	Name	MPa	m	μm	μm	MPa
Summers Byerlee 1977	Fig85-Evt11	398	0.0254	114	255	24.99
Summers Byerlee 1977	Fig85-Evt12	398	0.0254	130	220	23.56
Summers Byerlee 1977	Fig85-Evt13	398	0.0254	58	306	22.14
Summers Byerlee 1977	Fig85-Evt1	320	0.0254	421.9	569.6	64.93
Summers Byerlee 1977	Fig85-Evt2	320	0.0254	132.5	887	80.53
Summers Byerlee 1977	Fig85-Evt3	320	0.0254	110	682	77.07
Summers Byerlee 1977	Fig85-Evt4	320	0.0254	88	786	91.37
Summers Byerlee 1977	Fig85-Evt5	320	0.0254	78	727	79.96
Summers Byerlee 1977	Fig85-Evt6	320	0.0254	126	656	73.57
Summers Byerlee 1977	Fig85-Evt7	320	0.0254	82	665	71.36
Summers Byerlee 1977	Fig85-Evt1	240	0.0254	248.9	890.1	95.7
Summers Byerlee 1977	Fig85-Evt2	240	0.0254	76	1056	118.55
Summers Byerlee 1977	Fig85-Evt3	240	0.0254	199	1314	150.7
Summers Byerlee 1977	Fig85-Evt4	240	0.0254	165	1170	134.2
Summers Byerlee 1977	Fig85-Evt1	78	0.0254	403.2	837.8	98.52
Summers Byerlee 1977	Fig85-Evt2	78	0.0254	164	1039	122.79
Summers Byerlee 1977	Fig85-Evt3	78	0.0254	178	1162	136.4
Summers Byerlee 1977	Fig85-Evt4	78	0.0254	52	1051	117.84
Summers Byerlee 1977	Fig85-Evt5	78	0.0254	114	980	111.41
Summers Byerlee 1977	Fig86-Evt1	547	0.0254	255.7	928.3	104.44
Summers Byerlee 1977	Fig86-Evt2	547	0.0254	279	1229	145.73
Summers Byerlee 1977	Fig86-Evt3	547	0.0254	291	1414	161.23
Summers Byerlee 1977	Fig86-Evt4	547	0.0254	187	1246	138.03
Summers Byerlee 1977	Fig86-Evt1	630	0.0254	230	1214	117.02
Summers Byerlee 1977	Fig86-Evt2	630	0.0254	374	1875	204.62
Summers Byerlee 1977	Fig86-Evt3	630	0.0254	327	1555	177.32
Summers Byerlee 1977	Fig86-Evt1	547	0.0254	291	1414	161.23
Summers Byerlee 1977	Fig86-Evt2	547	0.0254	187	1246	138.03
Summers Byerlee 1977	Fig86-Evt1	630	0.0254	230	1214	117.02
Summers Byerlee 1977	Fig86-Evt2	630	0.0254	374	1875	204.62
Summers Byerlee 1977	Fig86-Evt3	630	0.0254	327	1555	177.32

Table S3. Data from Natural Earthquakes.

Earthquake	Detection Method	Reference	Coseismic Magnitude	Precursory Magnitude	Coseismic Moment	Precursory Moment
			Mw	Mw	N.m	N.m
2009 L'Aquila, IT	GPS	Borghini et al., 2016	6.30	5.90	3.59E+18	9.02E+17
2011 Tohoku-Oki, JP	Repeaters +GPS	Kato et al., 2012	9.00	7.03	3.16E+22	4.47E+19
2014 Iquique, CL	GPS	Socquet et al., 2017	8.10	7.12	1.80E+21	6.17E+19
2014 Papanaoa, MX	GPS	Radiguet et al., 2016	7.30	6.98	1.14E+20	3.78E+19
2015 Illapel, CL	Repeaters	Huang & Meng., 2018	8.40	6.83	5.07E+21	2.25E+19
2017 Valparaiso, CL	Repeaters +GPS	Ruiz et al., 2017	6.90	6.50	2.85E+19	7.16E+18
2012 Oxaca, MX	GPS	Graham et al., 2014	7.40	6.90	1.60E+20	2.85E+19
2001 Arequipa, PE	GPS	Ruegg et al., 2011	7.60	7.80	3.20E+20	6.38E+20
2012 Nicoya, CR	GPS	Voss et al., 2018	7.60	6.50	3.20E+20	2.81E+21
2004 Parkfield, USA	Deep Tremor	Shelly, 2009	6.00	4.90	1.27E+18	2.85E+16